Applied Mathematical Modelling 85 (2020) 318–337

Contents lists available at ScienceDirect

Applied Mathematical Modelling

journal homepage: www.elsevier.com/locate/apm

Non-Newtonian phase-change heat transfer of nano-enhanced octadecane with mesoporous silica particles in a tilted enclosure using a deformed mesh technique

Mohammad Ghalambaz[a,b,*], S.A.M. Mehryan[c], Ali Tahmasebi[d], Ahmad Hajjar[e]

[a] Metamaterials for Mechanical, Biomechanical and Multiphysical Applications Research Group, Ton Duc Thang University, Ho Chi Minh City, Vietnam
[b] Faculty of Applied Sciences, Ton Duc Thang University, Ho Chi Minh City, Vietnam
[c] Young Researchers and Elite Club, Yasooj Branch, Islamic Azad University, Yasooj, Iran
[d] Department of Mechanical Engineering, Shahid Chamran University of Ahvaz, Ahvaz, Iran
[e] ECAM Lyon, LabECAM, Université de Lyon, Lyon, France

ARTICLE INFO

Article history:
Received 6 October 2019
Revised 18 March 2020
Accepted 25 March 2020
Available online 15 May 2020

Keywords:
Deformed mesh technique
Mesoporous silica particles
Nano-enhanced phase change materials (NEPCMs)
Non-Newtonian flow
Phase change heat transfer

ABSTRACT

In the present study, the melting phase-change heat transfer of nano-enhanced phase-change octadecane by using mesoporous silica particles is investigated in an inclined cavity, theoretically. The presence of mesoporous silica particles induces non-Newtonian effects in the molten octadecane. A phase-change interface-tracking approach, deformed mesh technique, is employed to track the phase-change interface and heat transfer in the cavity. The Arbitrary Lagrangian-Eulerian (ALE) moving mesh technique along with the finite element method is adopted to solve the governing equations for conservation of mass, momentum, and energy during the phase-change process. A re-meshing technique and an automatic time step control approach are employed to control the quality of the deformed mesh and the computed numerical solution. The effect of various mass fractions of nanoparticles and various inclination angles of the enclosure on the heat transfer and phase-change behavior of nano-enhanced octadecane are addressed. The outcome reveals that using the mesoporous silica particles diminish the heat transfer in the enclosure. Although the presence of nanoparticles improved the conductive heat transfer, a reduction in the phase-change heat transfer performance of the enclosure can be observed, which is due to the increase of the viscosity (consistency parameter) of the liquid and suppression of natural convective flows. Moreover, the presence of nanoparticles reduces the latent heat capacity of octadecane as they do not contribute to the phase-change energy storage. Dispersing 5% mass fraction of nanoparticles in octadecane can reduce the heat transfer up to 50% and increase the consistency parameter by three folds. The angle of inclination of the cavity also plays an important role in the heat transfer characteristics. Tilting the cavity by -75° leads to an 80% reduction in the heat transfer.

* Corresponding author at: Ton Duc Thang University, Ho Chi Minh City, Vietnam.
E-mail address: mohammad.ghalambaz@tdtu.edu.vn (M. Ghalambaz).

https://doi.org/10.1016/j.apm.2020.03.046
0307-904X/

Nomenclature

Latin symbols

$\vec{f}$	volumetric force (N m^{-3})
$\vec{F}$	non-dimensional volumetric force
$\dot{G}$	non-dimensional shear strain rate
$\vec{u}$	velocity (m s^{-1})
$\vec{U}$	non-dimensional velocity
C_p	specific heat capacity at constant pressure (J kg^{-1} K^{-1})
F	deformation gradient
Fo	non-dimensional time (Fourier number)
g	gravity acceleration (m s^{-2})
h	volumetric convective heat transfer coefficient (W m^{-3} K^{-1})
I	unit matrix
J	determinant of the deformation gradient
k	thermal conductivity coefficient (W m^{-1} K^{-1})
L	cavity size (m)
L_h	latent heat of fusion (J kg^{-1})
m	consistency of dynamic viscosity (mPa s^n)
n	power-law index of the non-Newtonian fluid
$NMVF$	normalized melt volume fraction
Nu	Nusselt number
p	pressure (Pa)
P	non-dimensional pressure
Pr	Prandtl number
Ra	Rayleigh number
Ste	Stefan number
t	time (s)
T	temperature (K)
tr	transpose of the matrix
u, v	x and v velocity components (m s^{-1})
U, V	non-dimensional X and V velocity components
x, y	Cartesian coordinates (m)
X, Y	non-dimensional Cartesian coordinates

Greek symbols

$\dot{\gamma}$	shear strain rate (s^{-1})
α	thermal diffusivity (m^2 s^{-1})
β	thermal expansion coefficient (K^{-1})
θ	non-dimensional temperature
λ	inclination angle (degree)
μ	dynamic viscosity (kg m^{-1} s^{-1})
ν	kinematic viscosity (m^2 s^{-1})
ρ	density (kg m^{-3})
ϕ	volume fraction
ϕ_{wt}	mass fraction

Subscripts

0	initial value
avg	average property
c	Cold
f	fluid PCM
fu	Fusion
h	Hot
l	local property
nf	nano-PCM at fluid phase
np	nanoparticles
NP	nano-PCM
ns	nano-PCM at solid phase
s	solid PCM

1. Introduction

The quest for new energy resources and effective energy storage techniques has become one of the major concerns of this century due to the exponentially increasing demands in energy in the various industrial domains. In energy storage, Phase-change Materials (PCM) have drawn a lot of attention in the last few decades [1,2], as an alternative to other thermal storage techniques such as thermochemical reactions. PCM-based applications include the thermal management of buildings [3,4], air-conditioning systems [5], and electronic devices [6]. The main advantage offered by the PCM is their ability to provide a great amount of energy for a low-temperature variation, due to the latent heat of phase-change.

PCM absorbs or releases energy by melting or solidification when the surrounding temperature is close to its fusion temperature. Nonetheless, PCM has a low thermal conductivity, which presents a barrier slowing down heat transfer and reducing the overall efficiency. Different thermal conductivity enhancement techniques have then been proposed [7,8] and tested such as PCM encapsulation [9,10], the use of porous materials and foams [11–14], finned tubes [15], metallic fins [16], metallic matrix structures [17] and the use of electrically conductive PCM (Ghalambaz et al. [18]). Another enhancement technique consists in adding highly-conductive nanoparticles to the PCM in order to improve its thermal conductivity. The PCM containing the nanoparticles is called Nano-Enhanced PCM, abbreviated as NEPCM. This technique was first proposed and tested by Khodadadi et al. [19], who compared the solidification of water containing copper nanoparticles and found a higher heat release rate in the NEPCM compared to the conventional PCM. Subsequently, the impact of dispersing nanoparticles on the thermal performance of PCM has been addressed (Şahan et al. [20]).

Due to their improved thermal conductivity compared to conventional PCM, the use of the NEPCM has shown to be very effective in heat transfer enhancement in cooling applications, where the PCM undergoes solidification. Motahar et al. [21] performed experiments on a PCM containing TiO_2 particles occupying a cavity cooled from one vertical side and observed a higher heat transfer rate due to the dispersion of the nanoparticles. Sheikholeslami [22] tested various shapes of copper oxide nanoparticles dispersed in a PCM undergoing solidification in a complex shaped energy storage enclosure and noticed a higher solidification rate due to the presence of the nanoparticles. The numerical results of Sheikholeslami et al. [23] showed that adding copper oxide nanoparticles helps in the solidification of PCM in an enclosure with V-shaped fins. Sheikholeslami and Mahian [24] explored the effects of the magnetic field on the solidification of a NEPCM in a porous cavity and found that both the magnetic field and the nanoparticles contribute to the reduction of solidification time.

Nonetheless, the advantages of using NEPCM during melting have been more limited, especially when heat transfer is dominated by convection. In fact, the dispersion of nanoparticles in the PCM increases its viscosity and hinders convective heat transfer. This was reported in several works that pointed out this disadvantage. For instance, Ho and Gao [25] investigated experimentally the melting of Paraffin dispersed with Al_2O_3 in a vertical enclosure and concluded that increasing the mass fraction of the nanoparticles diminished the natural convection heat transfer in the melted region. Zeng et al. [26] reported similar observations in their experimental study of the melting of a NEPCM in a bottom-heated vertical cavity. Jourabian and Frahadi [27] analyzed numerically the melting of ice containing Cu nanoparticles and found that while raising the concentration of the nanoparticles increases the viscosity of the nanofluid, it hinders convective heat transfer. Feng et al. [28] studied the convection melting of ice-copper NEPCM. Their results indicated a larger melting zone but a lower heat transfer rate when the fraction of the nanoparticles of the NEPCM was increased. Bondareva et al. [29] studied the heat transfer characteristics of nano-enhanced n-octadecane in a finned heat sink numerically and found that the presence of nanoparticles improves the melting rate only in conduction-dominated heat transfer mode.

Similarly, Boukani et al. [30] investigated the melting of a NEPCM in partially-filled horizontal elliptical capsules numerically and noted that while increasing the nanoparticles fraction has no effect when the heat transfer is conduction-dominated, it reduces the heat transfer rate when convection takes over. Ghalambaz et al. [31] addressed the effect of using hybrid nanoparticles and found that water/Al-MgO hybrid NEPCM showed a faster fusion time compared to water/MgO NEPCM. Ghasemiasl et al. [32] modeled the melting of two different PCM with different melting points in a rectangular enclosure. They observed that while adding alumina particles to the two PCM reduced melting time, adding copper particles reduced solidification time. Arici et al. [33] numerically investigated the melting of a paraffin-alumina PCM in a partially heated and cooled square enclosure. Their results showed that the heat transfer enhancement was optimal for a 1% nanoparticle concentration in a bottom-heated enclosure, and this enhancement decreased for concentrations above 1%.

The works discussed above regarding the melting process in the rectangular enclosure were done under a condition that the gravity acceleration is parallel to the vertical walls. In many engineering applications, however, the surface of the chambers is not aligned with the orientation of the gravity field. Moreover, depending on the orientation, the tilted enclosure can augment or weaken the buoyancy-driven natural convection as one of the main factors influencing the melting rate. As a result, the impact of cavity incline on the melting characteristics is a crucial subject for many engineering designs. Several studies pointed out the effect of the orientation of the enclosure occupied by the NEPCM on the thermal performance. For instance, Kashani et al. [34] investigated numerically the solidification of a NEPCM in a wavy cavity and concluded that the surface waviness affects the solidification mechanism. A similar conclusion was reported by Abdollahzadeh and Esmaeilpour [35].

Jourabian et al. [36] simulated the melting process with convection in an inclined cavity heated on the left wall. Their results indicated that rotating the enclosure counterclockwise leads to a more dominant convective effect. Sharma et al. [37] used a trapezoidal cavity in their numerical simulation of the solidification of Cu-water nanofluid and observed a substantial improvement of the heat transfer performance compared to a rectangular cavity with the same internal area.

Kamkari et al. [38] performed several experiments on the melting of a PCM in a rectangular cavity with different inclination angles and pointed out the impact of the orientation on heat transfer in the cavity.

Zennouhi et al. [39] conducted numerical simulations of the effect of the inclination angle of a rectangular enclosure on the melting of PCM inside it. They found that rotating the enclosure from the vertical orientation, where the sidewall is heated, to the horizontal one, where the bottom wall is heated, increased the melting rate inside the cavity. Similarly, Zeng et al. [40] performed a numerical study of the melting process of lauric acid PCM in a rectangular enclosure with five different orientations and concluded that rotating the cavity can increase the total melting time by up to five times.

Dhaidan [41] reviewed the analytical, numerical and experimental investigations of nano-structures assisted PCM and pointed out to the effect of the geometry of the container on heat transfer mode and melting characteristics. In another study, Dhaidan [42] studied the melting of n-eicosane PCM inside triangular containers with two different orientations, the lower-base, and upper-base containers and noted that the melting rate in the upper-base container is higher than that in the lower-base container. Zaho et al. [43] conducted experiments on the melting process of a PCM in a tilted rectangular cavity with seven different inclination angles and noted the impact of the cavity inclination on the total melting time. More recently, Al Siyabi et al. [44] demonstrated numerically and experimentally the significant effect of inclination inside a cylindrical PCM storage system on the PCM temperature distribution and the PCM melting rate and profile.

Similarly, Yang et al. [45] showed in their experiments on the melting of a PCM in a rectangular cavity with four different inclination angles the substantial influence of the cavity orientation on the liquid-solid interface propagation and on the heat transfer rate. Iachachene et al. [46] performed a numerical study of the melting of a NEPCM in a trapezoidal cavity with two different orientations, by changing the locations of the lower and upper base. They concluded that the melting rate of the NEPCM showed that changing the cavity orientation substantially affected the melting rate of the PCM. Bondareva et al. [47] analyzed the heat and mass transfer in an inclined heat sink filled with a NEPCM and concluded that a faster melting is obtained when the inclination angle is greater than 90° with respect to the horizontal.

To summarize, the dispersion of nanoparticles in the PCM and the orientation of the cavity filled with PCM both play a role in the thermal performance. As the type of the nanoparticles also affects the heat transfer characteristics [22,31], testing the free convection of NEPCM in tilted cavities dispersed with novel types of nanoparticles is, therefore, essential to better understand the NEPCM thermal behavior and to broaden the selection spectrum of nanoparticles for various applications.

In this context, mesoporous silica nanoparticles have proven to be a promising additive for the enhancement of the thermal conductivity of PCM [48]. However, the contribution of such particles to the melting process in cavities remains unclear. It is also worth noting that most of the previous works dealing with the free convection of NEPCM have not taken into account the rheological behavior of the NEPCM, which was considered as a Newtonian fluid. Nonetheless, the PCM can exhibit a non-Newtonian behavior by the presence of mesoporous silica nanoparticles. The non-Newtonian behavior of phase change materials has been measured in samples containing mesoporous silica nanoparticles by Motahar et al. [48] and in some other phase change material [49].

The objective of the current paper is then twofold and consists of investigating the joint effect of dispersing mesoporous silica particles in non-Newtonian n-octadecane PCM, as well as the inclination of the PCM-filled cavity, on the PCM thermal performance. Moreover, an advanced deformed mesh technique is utilized to model the phase change at a precise fusion temperature.

2. Physics of the problem

The configuration considered in the present work is a 2D inclined enclosure, as schematically illustrated in Fig. 1. A constant temperature of T_h is imposed at the left wall of the enclosure. The opposite wall of the enclosure is kept at the lower and constant temperature of T_c. The other walls are adiabatic. The n-Octadecane, as the phase-change material, containing mesoporous silica ($MPSiO_2$) nanoparticles, occupies the enclosure. The melted n-Octadecane with the $MPSiO_2$ nanoparticles can act as a power-law non-Newtonian fluid [48]. The variation of the density of n-Octadecane due to phase change is only a few percent [30]. Hence, the volume change of the mixture during the melting process is considered to be zero, and the density of the PCM is the mean value of the PCM in the solid and liquid phases. The variation of density could be of interest in the manufacturing process of injection molding and mechanical design of enclosures, but such a small variation of density does not affect the thermal behavior of the enclosure.

The buoyancy forces are modeled using the Boussinesq approximation. The unsteady and incompressible governing partial differential equations for the hydrodynamic and thermal and behavior of a non-Newtonian flow are:

Continuity equation [50]:

$$\bar{\rho}_{NP}\nabla^* \cdot \vec{u} = 0 \tag{1}$$

Momentum equation [14,50]:

$$\bar{\rho}_{NP}\left[\frac{\partial \vec{u}}{\partial t} + (\vec{u}\cdot\nabla^*)\vec{u}\right] = \nabla^* \cdot \left[-pI + \mu_{nf}\left(\nabla^*\vec{u} + (\nabla^*\vec{u})^{tr}\right)\right] + \vec{f} \tag{2}$$

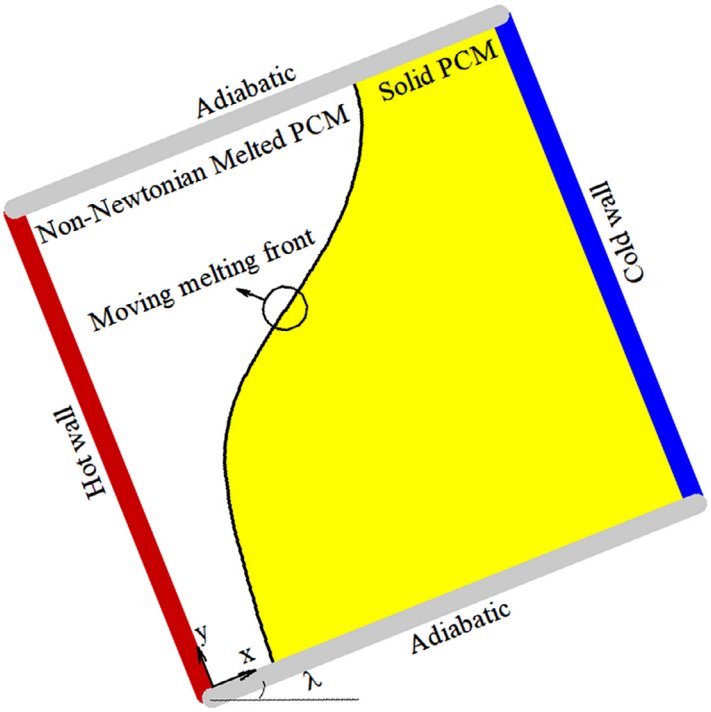

Fig. 1. A view of the physical model.

in which

$$\mu_{nf}(\dot{\gamma}) = m_{nf}\dot{\gamma}^{n_{nf}-1}\left|\begin{cases}\dot{\gamma} = \max\left(\sqrt{[D']:[D']}, \dot{\gamma}_{\min}\right)\\ 2D' = \left(\nabla\vec{u} + \left(\nabla\vec{u}\right)^{tr}\right)\end{cases}\right.$$

$$\vec{f} = f_x i + f_y j\left|\begin{array}{l} f_x = \overline{\rho}_{NP} g\beta_{nf}\left(T_{nf} - T_{fu}\right)\sin(\lambda)\\ f_y = \overline{\rho}_{NP} g\beta_{nf}\left(T_{nf} - T_{fu}\right)\cos(\lambda)\end{array}\right. \quad (3)$$

Energy equation in liquid [18,51]:

$$\bar{\rho}_{NP} C_{p,nf}\left[\frac{\partial T_{nf}}{\partial t} + \vec{u}\cdot\nabla^* T_{nf}\right] = \nabla^*\cdot\left(k_{nf}\nabla^* T_{nf}\right) \quad (4)$$

Energy equation in solid [51]:

$$\bar{\rho}_{NP} C_{p,ns}\frac{\partial T_{ns}}{\partial t} = \nabla^*\cdot\left(k_{ns}\nabla^* T_{ns}\right) \quad (5)$$

$\bar{\rho}_{NP}$ of the equations is the average density of the fluid and solid phases of the nano-PCM. The Stefan energy balance condition is applied to the position of the moving melting front [18]:

$$u = \frac{k_{nf}\frac{\partial T_{nf}}{\partial x} - k_{ns}\frac{\partial T_{ns}}{\partial x}}{(1-\phi)\bar{\rho}_{PCM} L_{h,PCM}} \quad (6a)$$

$$v = \frac{k_{nf}\frac{\partial T_{nf}}{\partial y} - k_{ns}\frac{\partial T_{ns}}{\partial y}}{(1-\phi)\bar{\rho}_{PCM} L_{h,PCM}} \quad (6b)$$

in which $\bar{\rho}_{PCM}$ is the average density of the liquid and solid PCM phases:

$$\bar{\rho}_{PCM} = \frac{\rho_{PCM,s} + \rho_{PCM,f}}{2} \quad (7)$$

Subscripts s and f denote the properties of the solid and fluid phases of the pure PCM.

The governing equations are subjected to the following boundary conditions:

Table 1
Thermal thermophysical properties of nano-PCM ($MPSiO_2$- octadecane) for various mass fractions of nanoparticles using experimental data [48].

Mass fraction (ϕ_{wt}) %	0.0	0.01	0.03	0.05
Volume fraction (ϕ) %	0.0	0.208	0.633	1.070
Power law index (n)	1	1	0.879	0.822
Consistency (m) [mPa.s^n]	3.536	3.987	7.910	11.021
Solid thermal conductivity (k_s) [W/m.K]	0.3706	0.3747	0.3834	0.3805
Liquid thermal conductivity (k_f) [W/m.K]	0.1521	0.1540	0.1570	0.1589

Table 2
Thermo-physical properties of the PCM and nanoparticles [30].

Property	n-Octadecane	Silica nanoparticles
Density (solid/liquid) [kg/m^3]	865 / 770	3970
Thermal expansion coefficient [1/K]	9.1×10^{-4}	0.63×10^{-5}
Specific heat capacity (solid / liquid) [J/kg.K]	1934 / 2196	765
Latent heat of fusion [kJ/kg]	243.5	-

The upper and lower boundaries:

$$\frac{\partial T(x,0)}{\partial y} = \frac{\partial T(x,L)}{\partial y} = 0, u = v = 0 \tag{8a}$$

The left boundary:

$$T(0,y) = T_h, u = v = 0 \tag{8b}$$

The right boundary:

$$T(L,y) = T_c, u = v = 0 \tag{8c}$$

The whole cavity is subjected to the following initial condition:

$$T = T_0, u = v = 0 \tag{8d}$$

Many nanofluids exhibit non-Newtonian effects due to the presence of nanoparticles. However, only a few studies investigated the non-Newtonian effects of nanoparticles in a suspension. Moreover, the theoretical models on the estimation of non-Newtonian behavior of nanofluids are imprecise and scarce. Hence, in the present study, the actual experimentally measured values of the consistency parameter (dynamic viscosity), power-law index, and the thermal conductivity are used for numerical computations. These thermophysical values are reported in the experimental research of Motahar et al. [48], who synthesized a sample of $MPSiO_2$-octadecane nano-enhanced PCM and reported the corresponding thermophysical properties. These thermophysical properties are summarized in Table 1 for various values of $MPSiO_2$ nanoparticle mass fractions. Hence, no theoretical or estimation relation were used for these important thermophysical properties, and instead, the actual measured values of these properties, which are reported in Table 1, are utilized.

The thermophysical properties of the nanoparticles and the host PCM are also tabulated in Table 2. The corresponding equations for the thermophysical properties of nano-PCM are a function of the volume fraction of nanoparticles. Hence, the transition from the mass fraction to the volume fraction is done through the following equation:

$$\phi = \frac{\bar{\rho}_{PCM}\phi_{wt}}{\phi_{wt}\bar{\rho}_{PCM} + (1-\phi_{wt})\rho_{np}} \tag{9}$$

The subscripts of *np* and *NP* are used for nanoparticles and nano-PCM properties, respectively.
The density of the nano-PCM:

$$\bar{\rho}_{NP} = (1-\phi)\bar{\rho}_{PCM} + \phi\rho_{np} \tag{10}$$

The heat capacity of nano-PCM:

$$\bar{\rho}_{NP}C_{p,nf} = \phi(\rho C_p)_{np} + (1-\phi)\bar{\rho}_{PCM}C_{p,f} \tag{11a}$$

$$\bar{\rho}_{NP}C_{p,ns} = \phi(\rho C_p)_{np} + (1-\phi)\bar{\rho}_{PCM}C_{p,s} \tag{11b}$$

The coefficient of volumetric thermal expansion for the liquid nano-PCM:

$$\bar{\rho}_{NP}\beta_{nf} = (1-\phi)\bar{\rho}_{PCM}\beta_f + \phi(\rho\beta)_{np} \tag{12}$$

The transition to the non-dimensional coordinates is conducted using the following correlations:

$$X = \frac{x}{L},\quad Y = \frac{y}{L},\quad U = \frac{uL}{\alpha_f}, V = \frac{vL}{\alpha_f}$$
$$\theta = \frac{T - T_{fu}}{T_h - T_{fu}}, P = \frac{L^2 p}{\bar{\rho}_{PCM}\alpha_f^2}, Fo = \frac{t\alpha_f}{L^2} \tag{13}$$

The non-dimensional equations based on the above correlations are as follows:

$$\nabla \cdot \vec{U} = 0 \tag{14}$$

$$\frac{\partial \vec{U}}{\partial Fo} + (\vec{U}\cdot\nabla)\vec{U} = \frac{\bar{\rho}_{PCM}}{\bar{\rho}_{NP}}\nabla\cdot\left[-PI + Pr\left[\frac{m_{nf}}{m_f}\frac{\alpha_f^{n_{nf}}}{\alpha_f^{n_f}}\frac{L^{2n_f}}{L^{2n_{nf}}}\right]\dot{G}^{n_{nf}-1}(\nabla\vec{U} + (\nabla\vec{U})^{tr}\right] + \vec{F} \tag{15}$$

In which

$$\vec{F} = F_X i + F_Y j \Big| F_X = \frac{\beta_{nf}}{\beta_f} RaPr\theta\sin(\lambda), F_Y = \frac{\beta_{nf}}{\beta_f} RaPr\theta\cos(\lambda)$$
$$\dot{G} = max\left(\sqrt{[D]:[D]}, \dot{G}_{min}\right) \Big| 2D = \left(\nabla\vec{U} + (\nabla\vec{U})^{tr}\right) \tag{16}$$

$$\frac{\partial\theta}{\partial Fo} + \left(\vec{U}\cdot\nabla\theta_{nf}\right) = \frac{\bar{\rho}_{PCM}C_{p,f}}{\bar{\rho}_{NP}C_{p,nf}}\left(\nabla\cdot\left(\frac{k_{nf}}{k_f}\nabla\theta_{nf}\right)\right) \tag{17}$$

$$\frac{\bar{\rho}_{NP}C_{p,ns}}{\bar{\rho}_{PCM}C_{p,f}}\frac{\partial\theta_{ns}}{\partial Fo} = \left(\nabla\cdot\left(\frac{k_{ns}}{k_f}\nabla\theta_{ns}\right)\right) \tag{18}$$

where Prandtl number *Pr*, and Rayleigh number *Ra* are as follows:

$$Pr = \frac{m_f}{\bar{\rho}_{PCM}}\frac{\alpha_f^{n_f-2}}{L^{2n_f-2}}, Ra = \frac{\bar{\rho}_{PCM}g\beta_f\Delta T L^{2n_f+1}}{m_f\alpha_f^{n_f}} \tag{19}$$

The velocity components of the moving interface in the non-dimensional form are obtained as:

$$U = \frac{1}{(1-\phi)}\left[\frac{k_{nf}}{k_f}\frac{\partial\theta_{nf}}{\partial X} - \frac{k_{ns}}{k_f}\frac{\partial\theta_{ns}}{\partial X}\right]Ste \tag{20a}$$

$$V = \frac{1}{(1-\phi)}\left[\frac{k_{nf}}{k_f}\frac{\partial\theta_{nf}}{\partial Y} - \frac{k_{ns}}{k_f}\frac{\partial\theta_{ns}}{\partial Y}\right]Ste \tag{20b}$$

in which Stefan number *Ste* is defined as:

$$Ste = \frac{C_{p,f}\Delta T}{L_{h,PCM}} \tag{20c}$$

As seen in Eq. (20), the volume fraction of nanoparticles appeared in the denominator of the interface velocity. This is because the presence of nanoparticles decreases the actual volume of the PCM, which could undergo a phase change and release/store latent heat. Thus, the increase of the volume fraction of nanoparticles reduces the overall latent heat of the PCM-mixture; hence, the movement of the interface accelerates by the increase of the nanoparticles' volume fraction. The thermal and dynamic conditions on the walls in the non-dimensional coordinates can be mentioned in the following forms:

The upper and lower boundaries:

$$\frac{\partial\theta(X,0)}{\partial Y} = \frac{\partial\theta(X,L)}{\partial Y} = 0, U = V = 0 \tag{21a}$$

The left surface:

$$\theta(0,Y) = 1, U = V = 0 \tag{21b}$$

The right surface:

$$\theta(1,Y) = \theta_c, U = V = 0 \tag{21c}$$

The whole domain is subjected to the initial conditions:

$$\theta = \theta_0, U = V = 0 \tag{21d}$$

It is to be noted that the initial temperature, T_0, is considered to be equal to the right boundary temperature, T_c. Thus, in the case of the non-dimensional form, $\theta_0 = \theta_c = \frac{T_c - T_{fu}}{T_h - T_{fu}} = -0.14$.

Here, the characteristics parameters are the normalized molten volume fraction as well as the heat transfer at the heated wall (Nusselt number). The molten volume fraction was normalized to the total PCM volume and computed as:

$$NMVF = \frac{\int_0^1 \int_0^{X_m} dXdY}{\int_0^1 \int_0^1 dXdY} \tag{22}$$

X_m of the above relation is the local horizontal distance of the moving interface from the vertical hot wall. Energy balance on the heated yields:

$$h(T - T_c) = -k_{nf} \frac{\partial T}{\partial x}\Big)_{x=0} \tag{23}$$

Invoking the non-dimensional variables, Eq. (23) leads to the local Nusselt number (Nu_l) as:

$$Nu_l = \frac{hL}{k_f} = \frac{k_{nf}}{k_f} \frac{\partial \theta}{\partial X}\bigg|_{X=0} \tag{24}$$

Finally, the average Nusselt number is obtained by integrating the local Nusselt number along the non-dimensional length of the heated:

$$Nu_{avg} = \int_0^1 Nu_l dY \tag{25}$$

3. Numerical method and mesh examination

The numerical simulation of the present work is built by a code applying the finite element method (FEM). The non-linear equations are first turned into the weak forms, and then interpolate or shape functions, $\{\gamma_k\}_{k=1}^N$, are utilized to expand the velocity, pressure, and temperature variables as follows:

$$U \approx \sum_{m=1}^{N} U_m \gamma_m(X,\ Y), V \approx \sum_{m=1}^{N} V_m \gamma_m(X,\ Y),\ P \approx \sum_{m=1}^{N} P_m \gamma_m(X,\ Y), \theta \approx \sum_{m=1}^{N} \theta_m \gamma_m(X,\ Y) \tag{26}$$

The Galerkin approach is employed, and the residual equations for the X and Y velocity components, as well as the pressure, and temperature are obtained at each element:

$$\begin{aligned} R_i^1 \approx & \sum_{m=1}^{N} U_m \int \frac{\partial \gamma_m}{\partial Fo} \gamma_i dXdY + \sum_{m=1}^{N} U_m \int \left[\left(\sum_{m=1}^{N} U_m \gamma_m \right) \frac{\partial \gamma_m}{\partial X} + \left(\sum_{m=1}^{N} V_m \gamma_m \right) \frac{\partial \gamma_m}{\partial Y} \right] \gamma_i dXdY \\ & - \frac{\bar{\rho}_{PCM}}{\bar{\rho}_{NP}} \sum_{m=1}^{N} \int \left(\sum_{m=1}^{N} P_m \gamma_m \right) \frac{\partial \gamma_m}{\partial X} \gamma_i dXdY + 2Pr \left[\frac{m_{nf}}{m_f} \frac{\alpha_f^{n_{nf}}}{\alpha_f^{n_f}} \frac{L^{2n_f}}{L^{2n_{nf}}} \right] \sum_{m=1}^{N} U_m \int \frac{\partial \gamma_i}{\partial X} \left(\dot{G}^{n_{nf}-1} \frac{\partial \gamma_m}{\partial X} dXdY \right) \\ & + Pr \left[\frac{m_{nf}}{m_f} \frac{\alpha_f^{n_{nf}}}{\alpha_f^{n_f}} \frac{L^{2n_f}}{L^{2n_{nf}}} \right] \sum_{m=1}^{N} U_m \int \frac{\partial \gamma_i}{\partial Y} \left(\dot{G}^{n_{nf}-1} \frac{\partial \gamma_m}{\partial Y} dXdY \right) + \frac{\beta_{nf}}{\beta_f} RaPr \sin(\lambda) \int \left(\sum_{m=1}^{N} \theta_m \gamma_m \right) \gamma_i dXdY \\ & + Pr \left[\frac{m_{nf}}{m_f} \frac{\alpha_f^{n_{nf}}}{\alpha_f^{n_f}} \frac{L^{2n_f}}{L^{2n_{nf}}} \right] \sum_{m=1}^{N} V_m \int \frac{\partial \gamma_i}{\partial Y} \left(\dot{G}^{n_{nf}-1} \frac{\partial \gamma_m}{\partial X} dXdY \right) \end{aligned} \tag{27a}$$

$$\begin{aligned} R_i^2 \approx & \sum_{m=1}^{N} V_m \int \frac{\partial \gamma_m}{\partial \tau} \gamma_i dXdY + \sum_{m=1}^{N} V_m \int \left[\left(\sum_{m=1}^{N} U_m \gamma_m \right) \frac{\partial \gamma_m}{\partial X} + \left(\sum_{m=1}^{N} V_m \gamma_m \right) \frac{\partial \gamma_m}{\partial Y} \right] \gamma_i dXdY \\ & - \frac{\bar{\rho}_{PCM}}{\bar{\rho}_{NP}} \sum_{m=1}^{N} \int \left(\sum_{m=1}^{N} P_m \gamma_m \right) \frac{\partial \gamma_i}{\partial Y} dXdY + 2Pr \left[\frac{m_{nf}}{m_f} \frac{\alpha_f^{n_{nf}}}{\alpha_f^{n_f}} \frac{L^{2n_f}}{L^{2n_{nf}}} \right] \sum_{m=1}^{N} V_m \int \frac{\partial \gamma_i}{\partial Y} \left(\dot{G}^{n_{nf}-1} \frac{\partial \gamma_m}{\partial Y} dXdY \right) \\ & + Pr \left[\frac{m_{nf}}{m_f} \frac{\alpha_f^{n_{nf}}}{\alpha_f^{n_f}} \frac{L^{2n_f}}{L^{2n_{nf}}} \right] \sum_{m=1}^{N} V_m \int \frac{\partial \gamma_i}{\partial X} \left(\dot{G}^{n_{nf}-1} \frac{\partial \gamma_m}{\partial X} dXdY \right) + \frac{\beta_{nf}}{\beta_f} RaPr \cos(\lambda) \int \left(\sum_{m=1}^{N} \theta_m \gamma_m \right) \gamma_i dXdY \\ & + Pr \left[\frac{m_{nf}}{m_f} \frac{\alpha_f^{n_{nf}}}{\alpha_f^{n_f}} \frac{L^{2n_f}}{L^{2n_{nf}}} \right] \sum_{m=1}^{N} U_m \int \frac{\partial \gamma_i}{\partial Y} \left(\dot{G}^{n_{nf}-1} \frac{\partial \gamma_m}{\partial X} dXdY \right) \end{aligned} \tag{27b}$$

Table 3
Mesh sizes in the studied domain.

Mesh cases Case No.	Number of melting interface elements (M)	Number of domain elements	$Fo = 1$	
			NMVF	*$Error$ (%)
I	50	2612	0.72347	0.177
II	100	4174	0.72545	0.097
III	**150**	**6370**	**0.72475**	**-**
IV	200	8948	0.72526	0.070
V	250	11320	0.72517	0.058

*$Error = |\frac{NMVF_{caseIII} - NMVF}{NMVF_{caseIII}}| \times 100$.

$$R_i^3 \approx \sum_{m=1}^{N} U_m \int \frac{\partial \gamma_m}{\partial X}\gamma_i dXdY + \sum_{m=1}^{N} V_m \int \frac{\partial \gamma_m}{\partial Y}\gamma_i dXdY \tag{27c}$$

$$\begin{aligned} R_i^4 \approx & \sum_{m=1}^{N} \theta_{nf_m} \int \frac{\partial \gamma_m}{\partial Fo}\gamma_i dXdY \\ & + \sum_{m=1}^{N} \theta_{nf_m} \int \left[\left(\sum_{m=1}^{N} U_m \gamma_m \right) \frac{\partial \gamma_m}{\partial X} + \left(\sum_{m=1}^{N} V_m \gamma_m \right) \frac{\partial \gamma_m}{\partial Y} \right] \gamma_m dXdY \\ & + \frac{\bar{\rho}_{PCM} C_{p,f}}{\bar{\rho}_{NP} C_{p,nf}} \frac{k_{nf}}{k_f} \sum_{m=1}^{N} \theta_{nf_k} \int \left[\frac{\partial \gamma_m}{\partial X}\frac{\partial \gamma_i}{\partial X} + \frac{\partial \gamma_m}{\partial Y}\frac{\partial \gamma_i}{\partial Y} \right] dXdY \end{aligned} \tag{27d}$$

Gaussian quadrature is applied to integrate the residual equations. The time step is selected automatically by utilizing the Backward Differentiation Formula (BDF) within a free time step between one and two. Newton method by using PARDISO solver is applied to solve the residual equations [52–54] iteratively. PARDISO is an open-source parallel solver with an excellent convergence rate. The iterations stop when the residual error reaches 10^{-6}, while the Newtonian damping factor of iterations is 0.8. The velocity components are used to obtain the streamline patterns.

The generated mesh is an unstructured mesh using Delaunay-based mesh generation available as open-source code as MESH2D function. Preparing the right mesh, as well as the mesh independence analysis, plays a prominent role in the achievement of plausible results in the numerical study. Accordingly, the triangular elements are used to discretize the studied domain consisting of two separate regions; the liquid melted PCM and the solid PCM. Indeed, the interface between the two regions is divided equally into M elements. By defining this controlled division, the unstructured mesh is applied to the whole domain. It is worth noting that the finer meshes are employed adjacent to the walls in the fluid region since the temperature and velocity gradients are substantial in these areas. A remeshing scheme based on the distortion of elements is utilized to ensure the quality of the utilized mesh during the computations. The first invariant of the isochoric Green–Lagrange strain is adopted as the mesh-distortion indicator in the 2D space. Hence, the remeshing will be performed when the following condition is satisfied:

$$\sqrt{\frac{\mathrm{tr}F^T F}{2J} - 1} > 1.2 \tag{28}$$

where F and J denote the deformation gradient and the determinant of the deformation gradient.

Five mesh sizes are tested, as shown in Table 3. This table shows that the results are within an accuracy of below 1%. Fig. 2 shows the variation of liquid fraction as a function of time for various mesh sizes at $Ra = 1.45 \times 10^6$, $Ste = 0.16$, $Pr = 51.7$, $\phi_{wt} = 0.05$, and $\lambda = 0°$. The results demonstrate that the mesh size of case III provides acceptable accuracy. Therefore, this mesh is confidently selected to conduct the numerical solution of the current work.

It is necessary to verify and validate the solution algorithm and its accuracy. Hence, the calculated results in this study are compared with those predicted and measured by several published papers in the literature. At the first evaluation, the natural convection flow of a power-law non-Newtonian fluid flowing inside an enclosed cavity, presented by Matin and Khan [55], is re-simulated. The average Nusselt numbers for the different values of the power-law index of the current calculations and those presented by Matin and Khan [55] are depicted in Fig. 3. Evidently, there is quite a satisfactory agreement between the results of Matin and Khan [55] and ours. Since the melting process can be dependent on the inclination angle of the enclosure, the calculated results of the current work and Cheong et al. [56] are compared as the next case. Cheong et al. [56] studied the natural convection flow of a Newtonian fluid in a rectangular cavity using the finite difference method. For the case of a rectangular cavity with $Ar = 1$ (aspect ratio) and $Pr = 0.71$, the average Nusselt numbers calculated in the current work and presented in Cheong et al. [56] for different values of the inclination angle of the enclosure and various Rayleigh numbers are depicted in Fig. 4. As shown, an excellent matching is observed.

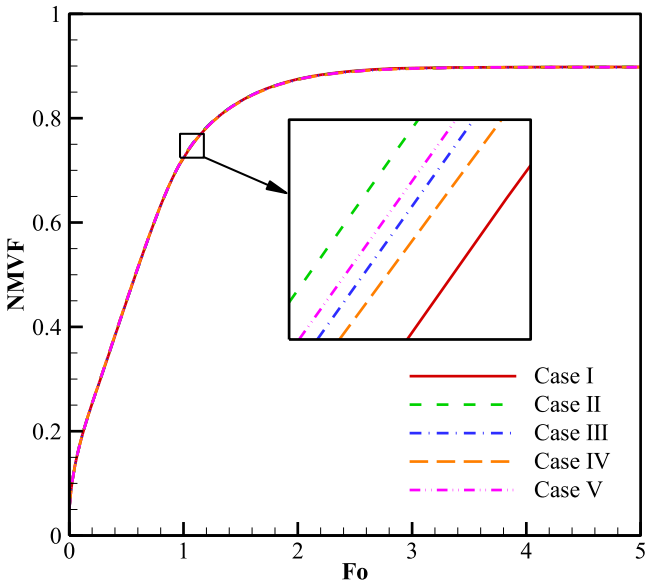

Fig. 2. Mesh independence analysis for $\phi_{wt} = 0.05$ and $\lambda = 0°$.

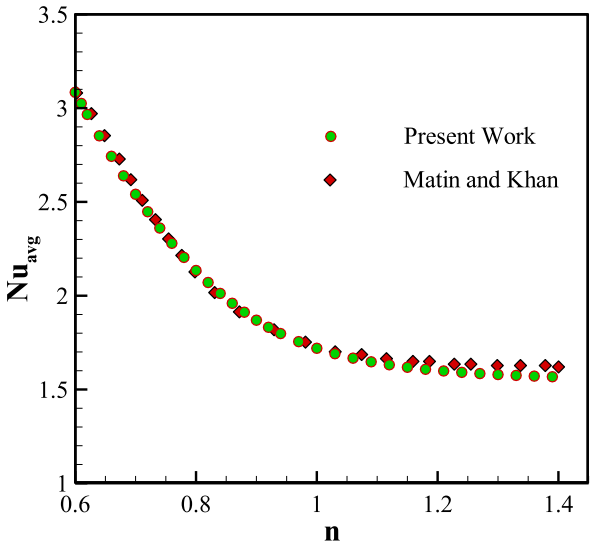

Fig. 3. Average Nusselt number against power-law index (n) of the current study (dash-dot) and Matin and Khan [55] (points) for $Ra = 10^3$ and $Pr = 10$.

To verify and validate the numerical modeling for the melting process, the melting fronts obtained using the current code and those depicted in [34,57,58] are compared for different values of the Fourier numbers. The melting process of a Newtonian PCM in a square cavity was conducted in [34,57,58]. The insulated horizontal bounds of the cavity and constant temperatures for vertical walls (i.e., higher temperature for the left wall and lower temperature for the right wall) were considered as the boundary conditions. Fig. 5 displays the comparison between the melting interfaces obtained from this study and those reported in [34,57,58]. Ultimately, the rates of buoyancy-driven heat transfer of a nanofluid flowing in a square enclosure are compared with the results of Kahveci [59]. In this work, Kahveci [59] investigated the buoyancy-driven heat transfer of a nanofluid of water and Al_2O_3 nanoparticles in a differentially heated cavity. As illustrated in Table 4, excellent matchings between our results and those of Kahveci [59] are observed.

4. Results and discussion

The current research aims to investigate the free convection melting process of nano-enhanced PCMs in an inclined cavity. The MPSiO_2-octadecane is adopted as the nano-enhanced PCM. Due to the presence of nanoparticles, the nano-enhanced PCM shows non-Newtonian behaviors. To obtain a feasible estimation of non-dimensional parameters, the size of the cavity

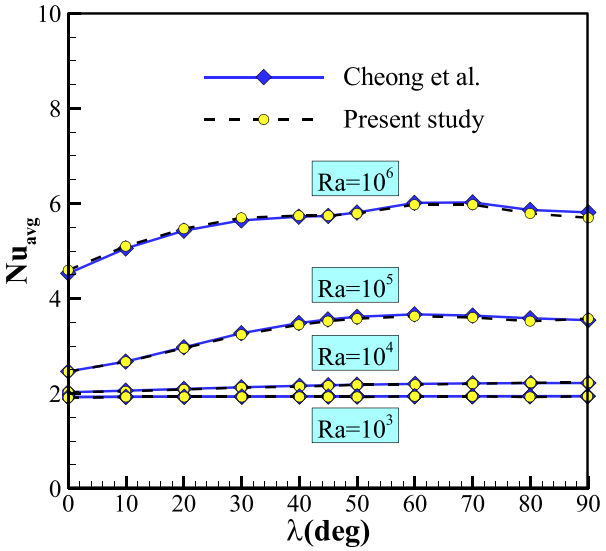

Fig. 4. The average Nusselt number of the present research and Cheong et al. [56].

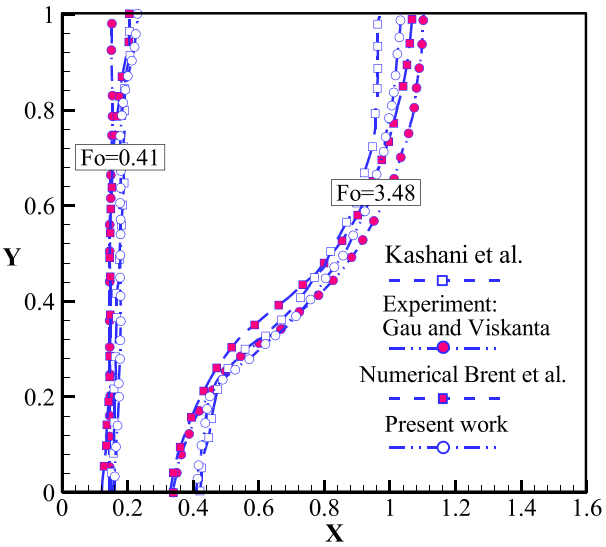

Fig. 5. The evaluated melting front of the present research and those of [34,57,58].

Table 4
The average Nusselt numbers of in the current research and the literature work [59] when $Ra = 10^6$.

	$\phi = 0$	$\phi = 0.05$	$\phi = 0.1$	$\phi = 0.15$
Present study	9.20	9.76	10.30	10.80
Kahveci	9.23	9.78	10.30	10.77

is adopted as 15 mm. The temperatures of the heated and cooled walls are set at $T_h = 45°C$ and $T_c = 25°C$, respectively. Also, the melting point is attained to be 27.5°C [48]. Furthermore, the initial thickness and the initial temperature of the liquid region in the cavity are considered to be 0.75 mm and 25°C, respectively. Invoking this case and using the thermo-physical properties of Tables 1 and 2, the non-dimensional parameters could be selected as $Ra = 1.45 \times 10^6$, $Ste = 0.16$, and $Pr = 51.7$. Moreover, the impact of suspending $MPSiO_2$ particles in the PCM and the inclination angle of the enclosure ($-75° \leq \lambda \leq +75°$) are investigated.

Fig. 6 shows the remeshing applied to the domain when the melting interface is moving with time. The red and blue colors (left and right subdomains) represent the liquid and solid regions, respectively. It is clear that the mesh is coarser

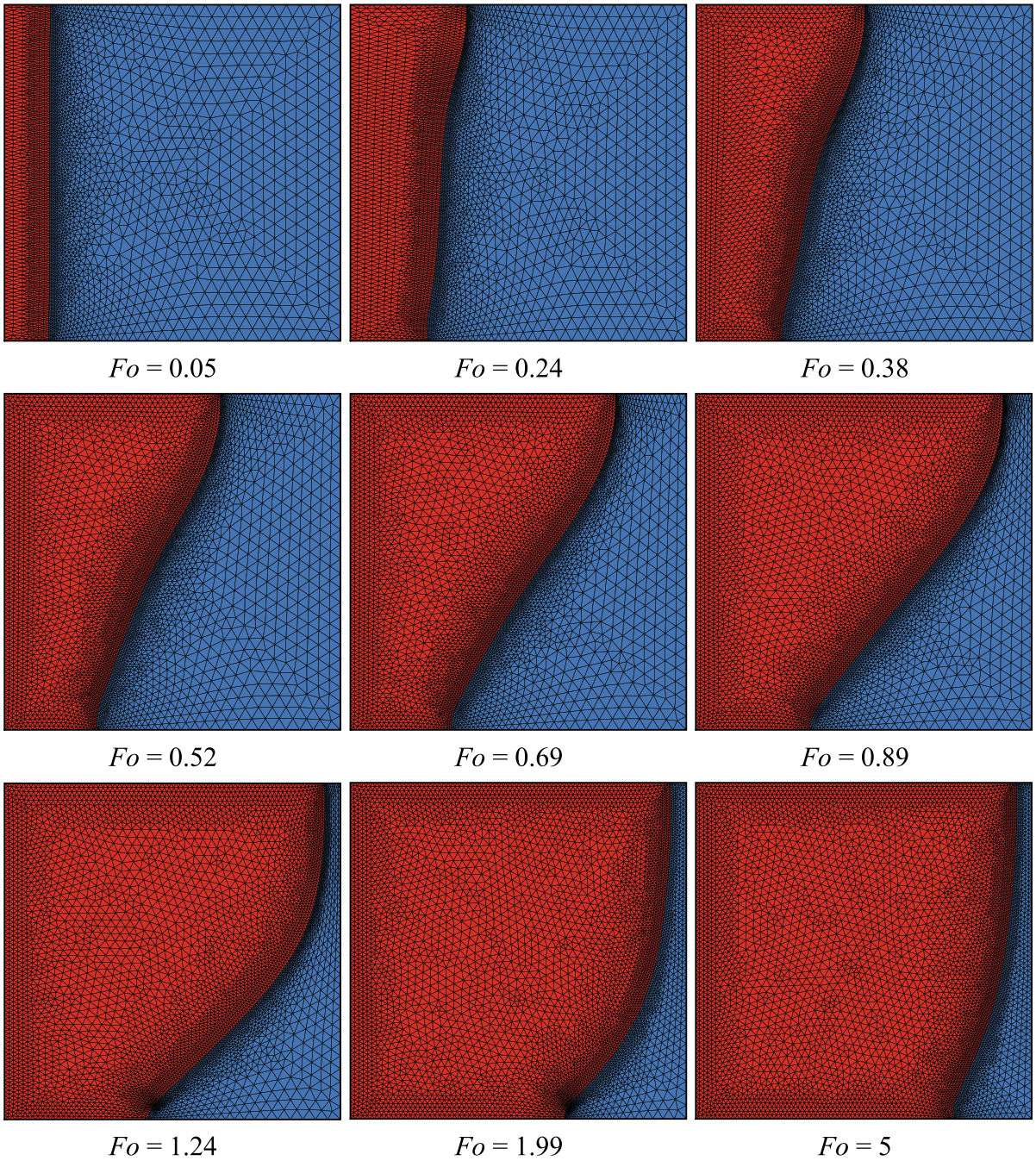

Fig. 6. The sequence of re-meshing during melting progress for $\phi_{wt} = 0.05$ and $\lambda = 0°$.

in the solid region compared to the liquid region, while the liquid-solid interface is subjected to further refinement. This is because there is a very weak conduction temperature gradient in the solid region and a coarse mesh can accurately capture such weak gradients. Using a coarse mesh at the solid region reduces the computational costs without losing the numerical accuracy. The size of the coarse meshes of the solid region was adjusted in the mesh examination process.

In the present work, the deformed mesh and re-meshing technique are employed to elevate the accuracy of the solution. Indeed, the re-meshing technique has been used to generate a new mesh configuration for the deformed mesh at each stage of the solution process whenever the mesh pattern provides inappropriate mesh quality owing to making so large

mesh deformation. Fig. 6 is prepared to show mesh deformation and the advancement of the melting interface during time. It can be seen that the mesh pattern continuously alters by progressing the melting process. The motion of the mesh by the deformation of the solid and liquid regions could stretch the mesh during the time and reduce its quality. Thus, by implementing the re-meshing technique, a new mesh pattern is generated to restore mesh quality and ensure accurate results. As seen in Fig. 6, all of the mesh views are regular without any notable distortion.

As the melting interface moves toward the cold wall, the mesh is adapted and refined in the liquid zone. This is due to the fact that the mechanism of heat transfer in the cavity is diffusion, and, thus, the temperature gradients in the solid region are insignificant compared to the liquid region. A mesh adaptation contributes to better accuracy of the results.

Fig. 7 illustrates the development of the streamlines and the isothermal contours with time for different values of the inclination angle λ. It is evident that the streamlines correspond to the liquid zone, as no flow is occurring in the solid zone. Initially, at $Fo = 0.15$, melting is limited to the region near the hot wall for all the values of *Fo*, as heat transfer is dominated by conduction. Later on, at $Fo = 0.45$, the melted PCM covers the left part of the cavity and convection dominates the heat transfer. For $\lambda = 75°$, the streamlines present a symmetry about the center.

For the other inclination angles, the streamlines present similar patterns, except for $\lambda = -75°$ where the melted zone is less limited near the top wall. Finally, at $Fo = 1.2$, the melted zone covers most of the cavity, except a limited region near the cold wall extended at the bottom. As the hot liquid near the top goes down along the melting front, it transfers its heat to the melting front and cools down. Consequently, melting near the bottom is substantially less than near the top. However, this behavior is not present for $\lambda = -75°$, where the melted zone stops near the center of the cavity, far from the cold wall and is almost vertical, indicating an equal melting rate between the top and the bottom. In fact, as the heat transfer is dominated by convection, the hot liquid circulates toward the top where melting is accelerated while cold liquid covers the bottom where heat transfer is inhibited. For $\lambda = -75°$, the heated wall is now closer to the upper vertical direction, and convective effects are almost uniform in the melted zone, leading thus to a more uniform melting interface compared to the other inclination angles.

On the other hand, comparing the isotherms for the different angles at $Fo = 1.2$ shows that while the contours are almost vertical for $\lambda = -75°$, they start to lean toward the center as λ is increased. For $\lambda = 0°$, the isotherms start near the hot wall and move quasi-horizontally in the center. As λ is further increased, the streamlines exhibit a similar behavior but are twisted in the cavity center. These observations suggest that while the inclination angle affects the temperature distribution in the cavity, it has a slight effect on the distribution of the streamlines unless the angle is strongly decreased.

The effect of the mass fraction of the nanoparticles, i.e., ϕ_{wt}, on the streamlines and the isotherms in the cavity at different instants is shown in Fig. 8. The melting starts near the hot wall and propagates until covering most of the cavity, except a narrow region near the cold wall at the top of the cavity and a larger region near the bottom. However, Fig. 8 shows that increasing ϕ_{wt} limits the size of the melted region for all the values of *Fo*. Indeed, the presence of a higher amount of nanoparticles affects the consistency of the melted PCM and slows down its circulation, and consequently inhibits convective heat transfer. In addition, ϕ_{wt} affects the form of streamlines. For instance, when $\phi_{wt} = 0$, the streamlines present a symmetry around the center, while this symmetry is not present for $\phi_{wt} = 0.05$, where the melted zone is shorter. Conversely, ϕ_{wt} has a limited impact on the isotherms, which present very similar contours when ϕ_{wt} is varied. Therefore, growing the mass fraction of the nanoparticles diminishes the extent of the melted zone but has little effect on the temperature distribution inside the cavity.

To better assess the impact of the inclination angle, the progress of the melting front for different values of *Fo* is depicted in Fig. 9 for different inclination angles λ. When the cavity is tilted in the anti-clockwise direction, the melting front is not greatly affected. When λ is increased to 75°, the melting font is less developed near the top while being more developed near the bottom. However, increasing λ to 30° rises the melting depth near the bottom but keeps it the same near the top. On the other hand, when the cavity is tilted in the clockwise direction, i.e. when λ is negative and decreased, the melting front shows a different variation. Initially, at $Fo = 0.15$, the melting front is not affected by λ and is almost the same in the different configurations.

For higher values of *Fo*, the melting front is less developed except in a small zone near the bottom. As previously explained, this is due to the fact that buoyancy effects are less effective when the heated wall is moved towards the upper vertical direction. For instance, if λ was decreased to -90°, the heated wall would be the top wall, and a horizontal melting front would be expected. These results indicate that while inclining the cavity in the anti-clockwise direction does not have a significant impact on the progress of the melting front location, tilting it in the clockwise direction tends to diminish the growth of the melting zone due to the reduction of convective effects.

Further analysis of the role of the mass fraction of the nanoparticles is conducted by plotting the location of the melting front location for different values of ϕ_{wt} and *Fo* as illustrated in Fig. 10. It is clear that for all the values of *Fo*, the increase of ϕ_{wt} to 3 and 5% reduces the development of the melting interface and the size of the melting zone. Nonetheless, the small increase in ϕ_{wt} to 1% does not affect the melting front, which remains almost the same as the case with no nanoparticles. In fact, nanoparticles do not contribute to latent heat. Growing the nanoparticles fraction decreases the amount of the PCM, and consequently decreases the contribution of latent heat to the overall heat transfer in the cavity. As heat transfer is decreased, melting is hindered, and the advancement of the melting interface is limited.

Fig. 11 shows the effect of the inclination angle, i.e. λ, on the variation of the normalized melting volume fraction *NMVF* and Nusselt number Nu_{avg} as a function of time. Initially, as illustrated in Fig. 11 (a), *NMVF* is the same in all the configurations, as the heat transfer in the first stage is dominated by conduction, and the role of convection is limited. As *Fo*

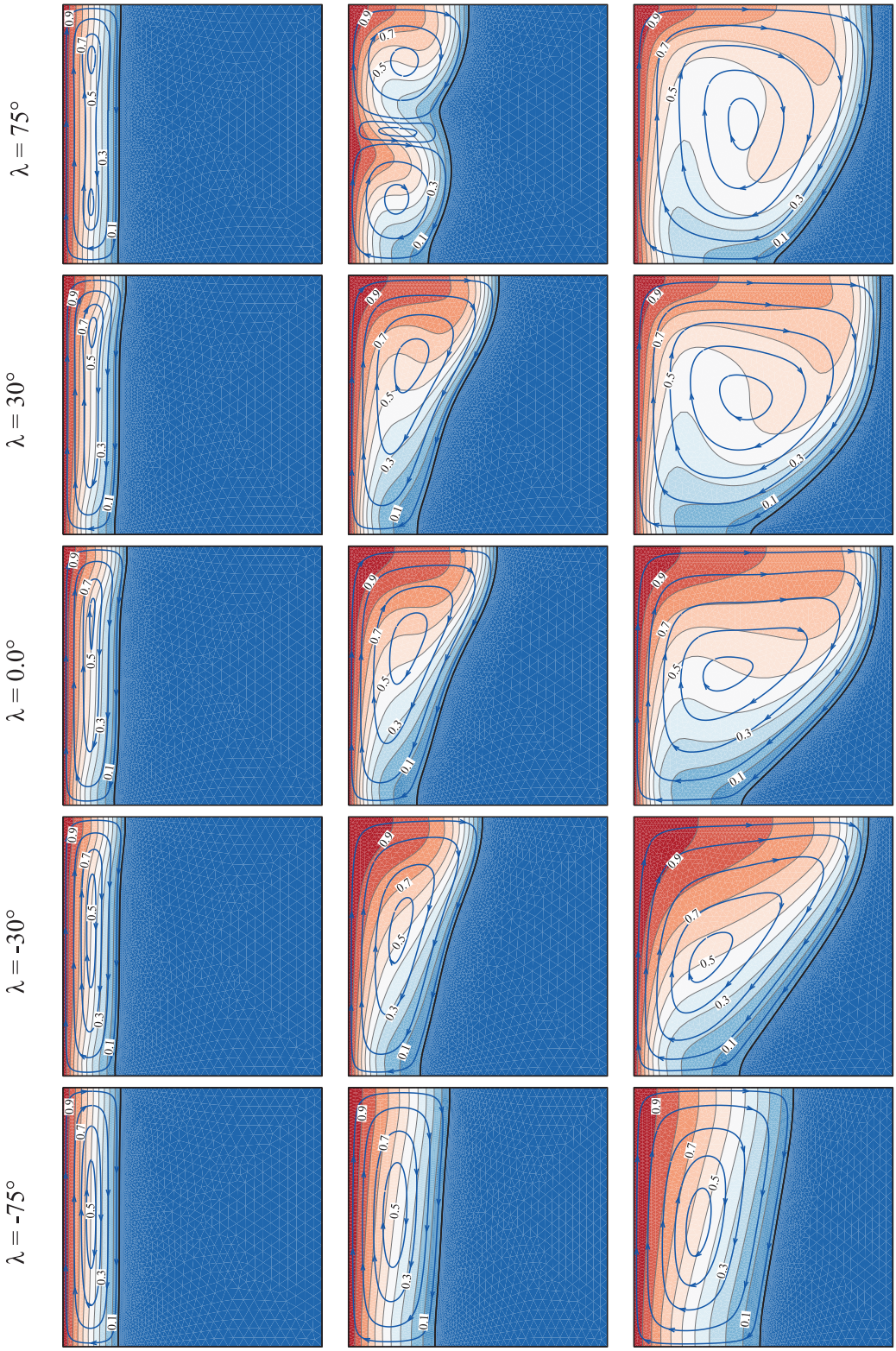

Fig. 7. Streamlines and isotherms at three selected Fourier number (Fo) for constant $\phi_{wt} = 0.05$ and different inclination angles (λ).

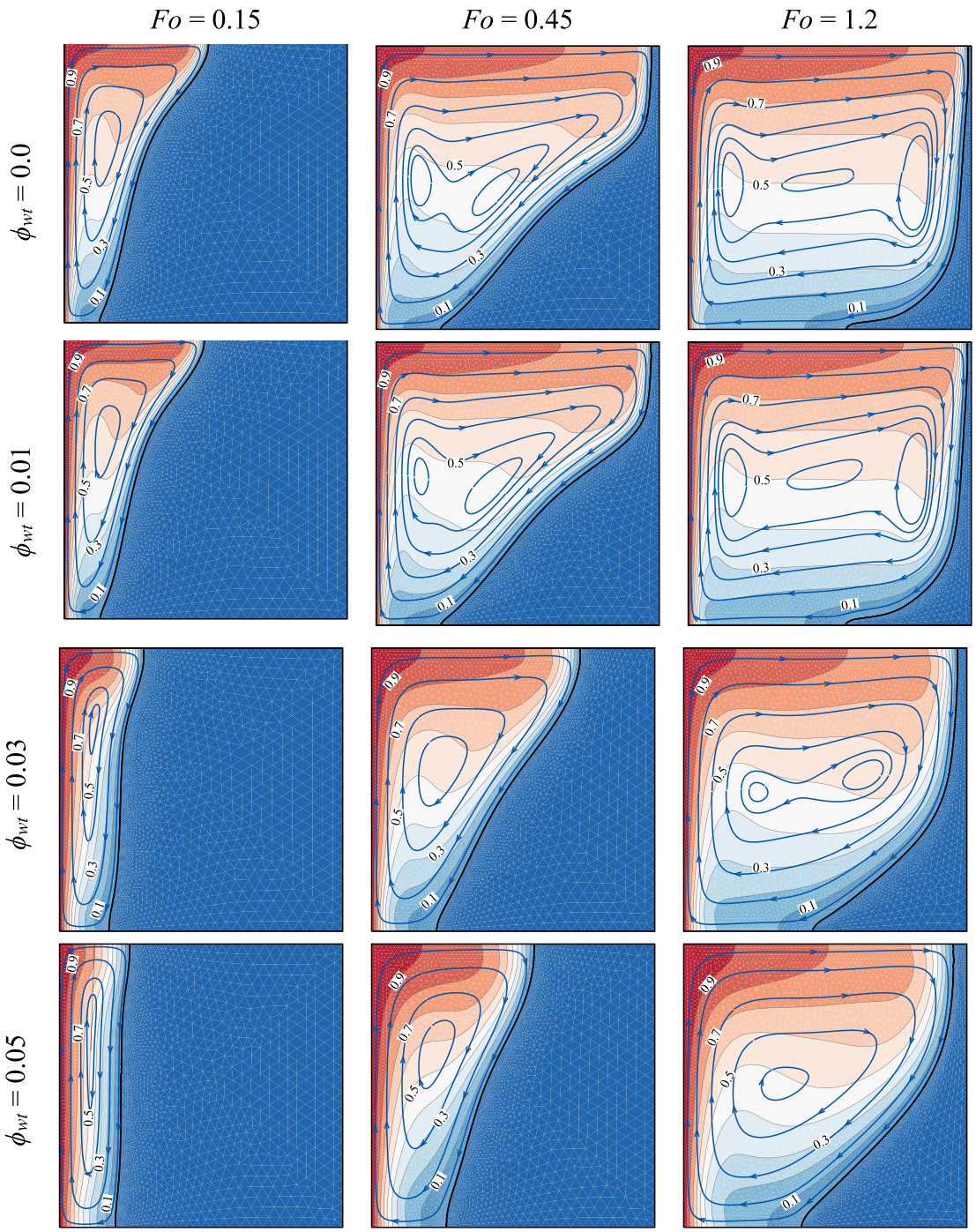

Fig. 8. Streamlines and isotherms at three selected Fourier number (Fo) for constant $\lambda = 0°$ and different mass fractions (ϕ_{wt}).

increases, the convection starts taking over a heat transfer mechanism, and the effect of the cavity inclination appears. As discussed earlier, tilting the cavity in the clockwise direction limits the convective effects and as a consequence, less PCM is melting, and *NMVF* is reduced. Tilting the cavity in the opposite direction does not, however, affect *NMVF*. The same effect appears in Fig. 11(b), where Nu_{avg} decreases significantly to 20% of its initial value when λ is reduced to -75°, indicating a diminished heat transfer.

On the other hand, Nu_{avg} slightly rises when λ is increased to 30° and remains constant for $\lambda = 75°$. These results confirm the fact that heat transfer is reduced when the cavity is tilted in the clockwise direction and are consistent with

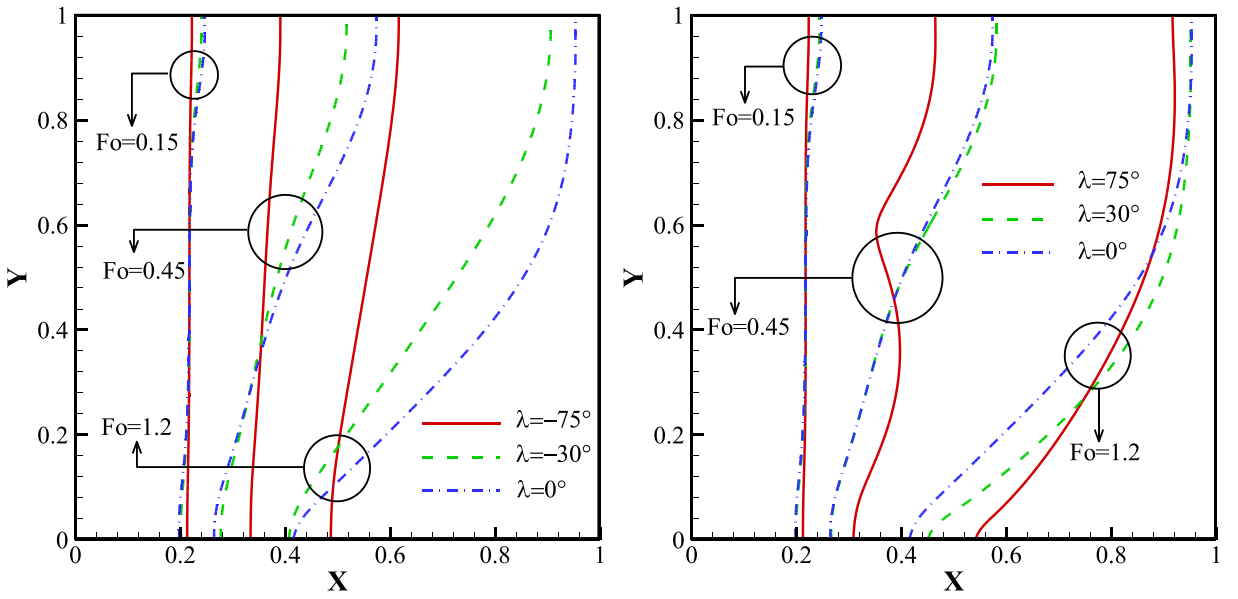

Fig. 9. Melting front surface under different inclination angles (λ) and Fourier numbers (*Fo*) for constant $\phi_{wt} = 0.05$.

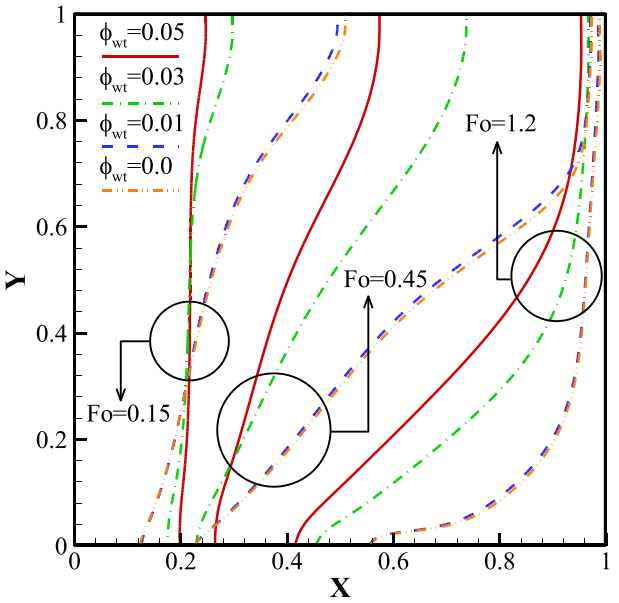

Fig. 10. Melting front surface under different mass fractions (ϕ_{wt}) and Fourier numbers (*Fo*) for constant $\lambda = 0°$.

the findings of [36,39,40] who obtained similar conclusions for the melting of a Newtonian PCM. The trend of the results for the inclination angle of the enclosure is in agreement with the literature works [34–47] for the case of a Newtonian phase change heat transfer.

The variation of *NMVF* as a function of time for different values of ϕ_{wt} is shown in Fig. 12(a). Similarly, Fig. 12(b) illustrates the variation of (1-ϕ) *NMVF*, representing the actual amount of PCM that went through phase-change and released heat, as a function of time. It is shown that *NMVF* is reduced when increasing ϕ_{wt} to 3 and 5%, and remains constant for $\phi_{wt} = 1\%$, indicating that the increase of ϕ_{wt} inhibits the PCM melting. The variation of the average Nusselt number as a function of time for different values of ϕ_{wt}, depicted in Fig. 13, confirms the previous observation and points out to the reduction of heat transfer due to the increase of ϕ_{wt}. A 5% value of ϕ_{wt} reduces Nu_{avg} by almost 50%. In fact, while the increase of the nanoparticles fraction enhances the thermal conductivity of the PCM and reduces the power index, it

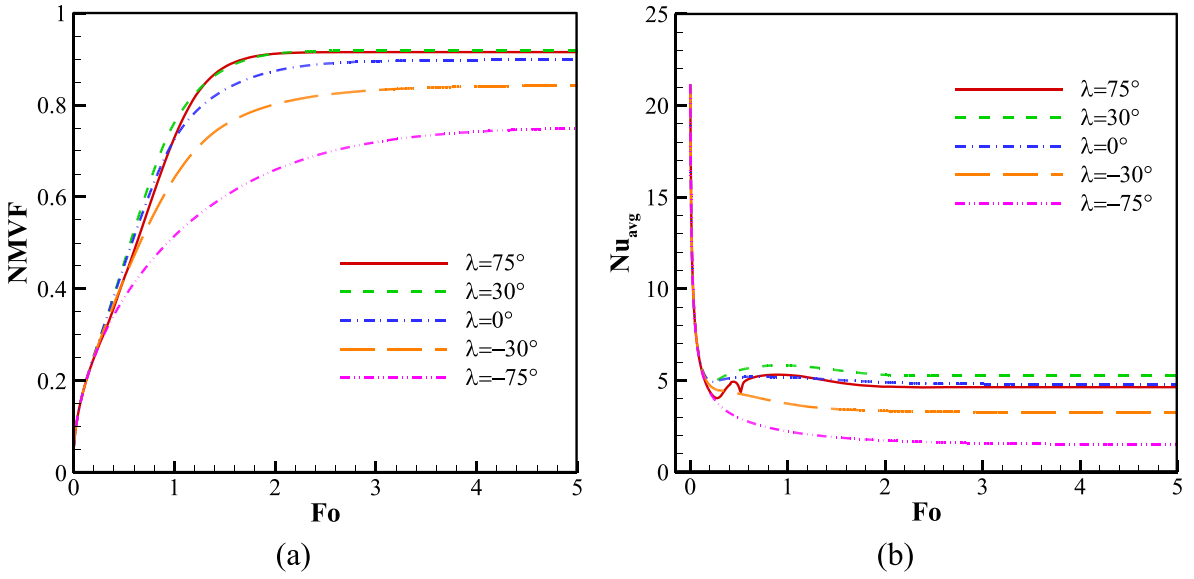

Fig. 11. (a): Normalized melting volume fraction and (b): average Nusselt number as a function of Fourier number (*Fo*) for different inclination angles (λ) and constant $\phi_{wt} = 0.05$.

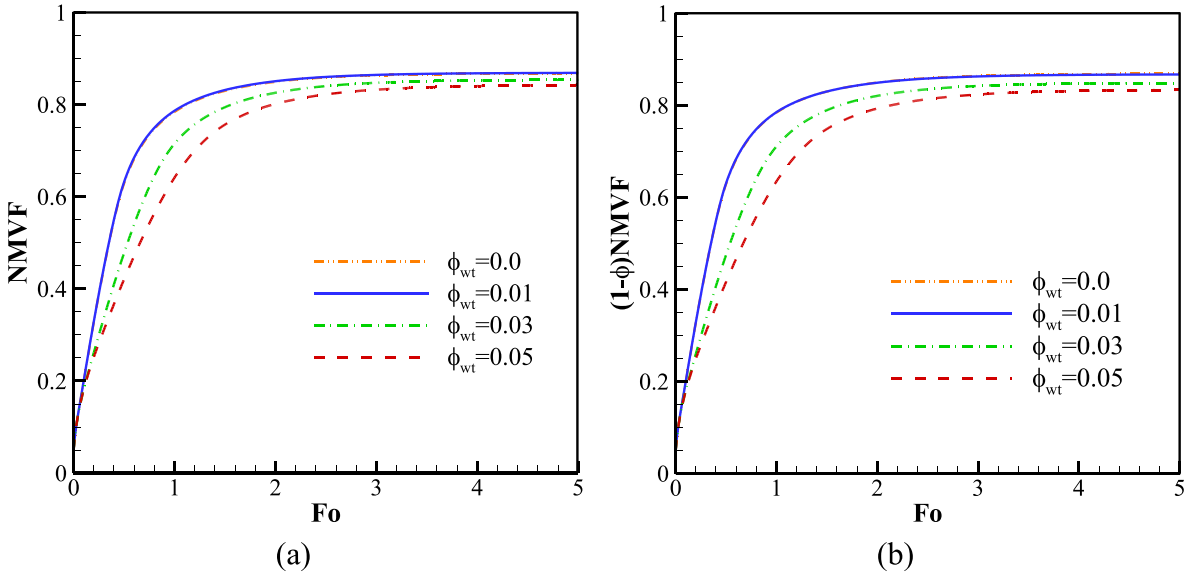

Fig. 12. (a): Normalized melting volume fraction, (b) melting volume fraction of PCM as a function of Fourier number (*Fo*) for different mass fractions (ϕ_{wt}) and constant λ = -30°.

also increases the consistency parameter, thus suppressing the convection and inhibiting heat transfer. These findings are in agreement with the results of several studies which pointed out that increasing ϕ_{wt} inhibits heat transfer due to the increased viscosity of the PCM [25-29]. The slight difference is that in the present work, the PCM is a non-Newtonian fluid, and therefore, the rise of the consistency parameter, which diminishes the free convective heat transfer.

Looking at Table 1 shows that the addition of the nanoparticles only slightly increases the thermal conductivity, which positively contributes to heat transfer enhancement. However, an increase of 200% and 300% in the consistency parameter is observed when the fraction of the particles is 3% and 5%, respectively. This increase slows down the natural convection and results in a lower heat transfer and a lower *NMVF*. To summarize, the positive contribution of the nanoparticle's conductivity to the heat transfer enhancement does not compensate for the negative effect resulting from the increase of the consistency parameter, and, overall, increasing the nanoparticles fraction in the PCM diminishes heat transfer in the cavity.

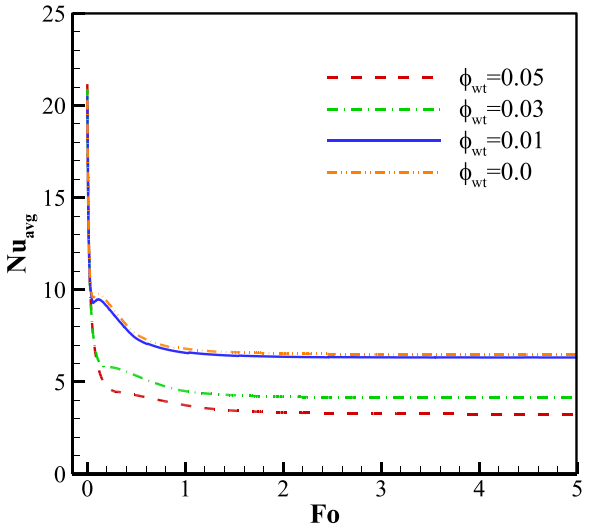

Fig. 13. Average Nusselt number as a function of Fourier number (Fo) for different mass fractions (ϕ_{wt}) and constant $\lambda = -30°$.

5. Conclusion

The melting free convection heat transfer of NEPMCs in an inclined cavity was addressed using a deformed mesh approach. The melting interface was tracked using the Stefan boundary condition. The presence of mesoporous silica particles induces non-Newtonian behavior in the liquid PCM. The finite element method was employed to solve the governing equation in the ALE moving mesh frame. The influence of various mass fractions of mesoporous silica particles on the melting volume fraction and heat transfer were investigated. The main results of the present investigation can be summarized as follows:

Changing the cavity inclination affects the streamline patterns and the temperature distribution inside the cavity. When the cavity is tilted in the clockwise direction, the hot wall is moved from the left side towards the top, and the convective effects are inhibited, leading to a lower melting volume fraction and a reduced heat transfer. When the cavity is tilted by -75°, an 80% reduction in heat transfer is observed. On the other side, inclining the cavity in the anti-clockwise direction does not have a noticeable effect on heat transfer and the melting volume fraction.

Increasing the fraction of the nanoparticles improves the thermal conductivity slightly, which contributes to heat transfer enhancement. However, an increase in the volume fraction of the nanoparticles presents several drawbacks. The main one is that when the nanoparticle fraction is increased, the consistency parameter rises and tends to suppress the natural convection. In particular, using a 3% mass fraction of nanoparticles raised the consistency parameter by 300%. Moreover, as the nanoparticles do not contribute to latent heat, the presence of nanoparticles diminishes the overall PCM material. Raising the nanoparticles fraction to 5% reduces the heat transfer by 50%.

In the present study, it was found that the presence of mesoporous silica particles can reduce heat transfer. Although the presence of nanoparticles improves the thermal conductivity, it reduces the natural convection effects by increasing the viscosity of the suspension. There are many applications such as macro capsules of PCMs or composites of PCMs, in which the natural convection effects are minimal. Maybe, in such cases, using nanoparticles improves the heat transfer due to conduction mechanisms, which can be addressed in future works.

Acknowledgment

Authors wish to sincerely appreciate the help, constructive comments, and corrections of Prof. Ali Chamkha during the revision of the manuscript.

Supplementary materials

Supplementary material associated with this article can be found, in the online version, at doi:10.1016/j.apm.2020.03.046.

References

[1] H. Nazir, M. Batool, F.J.B. Osorio, M. Isaza-Ruiz, X. Xu, K. Vignarooban, P. Phelan, A.M. Kannan, Recent developments in phase change materials for energy storage applications: A review, Int. J. Heat Mass Transfer 129 (2019) 491–523.

[2] Y. Tao, Y.-L. He, A review of phase change material and performance enhancement method for latent heat storage system, Renewable Sustainable Energy Rev. 93 (2018) 245–259.

[3] A.N. Keshteli, M. Sheikholeslami, Nanoparticle enhanced PCM applications for intensification of thermal performance in building: a review, J. Mol. Liq. (2018).
[4] F. Souayfane, F. Fardoun, P.-H. Biwole, Phase change materials (PCM) for cooling applications in buildings: A review, Energy Build. 129 (2016) 396–431.
[5] P. Moreno, C. Solé, A. Castell, L.F. Cabeza, The use of phase change materials in domestic heat pump and air-conditioning systems for short term storage: A review, Renewable Sustainable Energy Rev. 39 (2014) 1–13.
[6] K. Pielichowska, K. Pielichowski, Phase change materials for thermal energy storage, Prog. Mater Sci. 65 (2014) 67–123.
[7] Z.A. Qureshi, H.M. Ali, S. Khushnood, Recent advances on thermal conductivity enhancement of phase change materials for energy storage system: a review, Int. J. Heat Mass Transfer 127 (2018) 838–856.
[8] Y. Lin, Y. Jia, G. Alva, G. Fang, Review on thermal conductivity enhancement, thermal properties and applications of phase change materials in thermal energy storage, Renewable Sustainable Energy Rev. 82 (2018) 2730–2742.
[9] S. Demirbağ, S.A. Aksoy, Encapsulation of phase change materials by complex coacervation to improve thermal performances and flame retardant properties of the cotton fabrics, Fibers Polym. 17 (2016) 408–417.
[10] V. De Matteis, A. Cannavale, F. Martellotta, R. Rinaldi, P. Calcagnile, F. Ferrari, U. Ayr, F. Fiorito, Nano-encapsulation of phase change materials: From design to thermal performance, simulations and toxicological assessment, Energy Build. 188 (2019) 1–11.
[11] W. Alshaer, S. Nada, M. Rady, C. Le Bot, E.P. Del Barrio, Numerical investigations of using carbon foam/PCM/Nano carbon tubes composites in thermal management of electronic equipment, Energy Convers. Manage. 89 (2015) 873–884.
[12] T.-u. Rehman, H.M. Ali, M.M. Janjua, U. Sajjad, W.-M. Yan, A critical review on heat transfer augmentation of phase change materials embedded with porous materials/foams, Int. J. Heat Mass Transfer 135 (2019) 649–673.
[13] M. Ghalambaz, K.A. Ayoubloo, A. Hajjar, Melting heat transfer of a non-Newtonian phase change material in a cylindrical vertical-cavity partially filled porous media, Int. J. Numer. Methods Heat Fluid Flow (2019).
[14] S. Mehryan, M.H. Heidarshenas, A. Hajjar, M. Ghalambaz, Numerical study of melting-process of a non-Newtonian fluid inside a metal foam, Alexandria Eng. J. (2019).
[15] K. Ermis, A. Erek, I. Dincer, Heat transfer analysis of phase change process in a finned-tube thermal energy storage system using artificial neural network, Int. J. Heat Mass Transfer 50 (2007) 3163–3175.
[16] R. Baby, C. Balaji, Thermal optimization of PCM based pin fin heat sinks: an experimental study, Appl. Therm. Eng. 54 (2013) 65–77.
[17] Z. Li, Z.-G. Wu, Numerical study on the thermal behavior of phase change materials (PCMs) embedded in porous metal matrix, Sol. Energy 99 (2014) 172–184.
[18] M. Ghalambaz, S.H. Zadeh, S. Mehryan, I. Pop, D. Wen, Analysis of melting behavior of PCMs in a cavity subject to a line source magnetic field using a moving grid technique, Appl. Math. Modell. (2019).
[19] J. Khodadadi, S. Hosseinizadeh, Nanoparticle-enhanced phase change materials (NEPCM) with great potential for improved thermal energy storage, Int. Commun. Heat Mass Transfer 34 (2007) 534–543.
[20] N. Şahan, M. Fois, H. Paksoy, Improving thermal conductivity phase change materials—A study of paraffin nanomagnetite composites, Sol. Energy Mater. Sol. Cells 137 (2015) 61–67.
[21] S. Motahar, A.A. Alemrajabi, R. Khodabandeh, Experimental investigation on heat transfer characteristics during melting of a phase change material with dispersed TiO2 nanoparticles in a rectangular enclosure, Int. J. Heat Mass Transfer 109 (2017) 134–146.
[22] M. Sheikholeslami, Finite element method for PCM solidification in existence of CuO nanoparticles, J. Mol. Liq. 265 (2018) 347–355.
[23] M. Sheikholeslami, R.-u. Haq, A. Shafee, Z. Li, Heat transfer behavior of nanoparticle enhanced PCM solidification through an enclosure with V shaped fins, Int. J. Heat Mass Transfer 130 (2019) 1322–1342.
[24] M. Sheikholeslami, O. Mahian, Enhancement of PCM solidification using inorganic nanoparticles and an external magnetic field with application in energy storage systems, J. Cleaner Prod. 215 (2019) 963–977.
[25] C.-J. Ho, J. Gao, An experimental study on melting heat transfer of paraffin dispersed with Al2O3 nanoparticles in a vertical enclosure, Int. J. Heat Mass Transfer 62 (2013) 2–8.
[26] Y. Zeng, L.-W. Fan, Y.-Q. Xiao, Z.-T. Yu, K.-F. Cen, An experimental investigation of melting of nanoparticle-enhanced phase change materials (NePCMs) in a bottom-heated vertical cylindrical cavity, Int. J. Heat Mass Transfer 66 (2013) 111–117.
[27] M. Jourabian, M. Farhadi, Melting of nanoparticles-enhanced phase change material (NEPCM) in vertical semicircle enclosure: numerical study, J. Mech. Sci. Technol. 29 (2015) 3819–3830.
[28] Y. Feng, H. Li, L. Li, L. Bu, T. Wang, Numerical investigation on the melting of nanoparticle-enhanced phase change materials (NEPCM) in a bottom-heated rectangular cavity using lattice Boltzmann method, Int. J. Heat Mass Transfer 81 (2015) 415–425.
[29] N.S. Bondareva, B. Buonomo, O. Manca, M.A. Sheremet, Heat transfer inside cooling system based on phase change material with alumina nanoparticles, Appl. Therm. Eng. 144 (2018) 972–981.
[30] N.H. Boukani, A. Dadvand, A.J. Chamkha, Melting of a Nano-enhanced Phase Change Material (NePCM) in partially-filled horizontal elliptical capsules with different aspect ratios, Int. J. Mech. Sci. 149 (2018) 164–177.
[31] M. Ghalambaz, A. Doostani, E. Izadpanahi, A. Chamkha, Phase-change heat transfer in a cavity heated from below: the effect of utilizing single or hybrid nanoparticles as additives, J. Taiwan Inst. Chem. Eng. 72 (2017) 104–115.
[32] R. Ghasemiasl, S. Hoseinzadeh, M. Javadi, Numerical analysis of energy storage systems using two phase-change materials with nanoparticles, J. Thermophys. Heat Transfer 32 (2017) 440–448.
[33] M. Arıcı, E. Tütüncü, M. Kan, H. Karabay, Melting of nanoparticle-enhanced paraffin wax in a rectangular enclosure with partially active walls, Int. J. Heat Mass Transfer 104 (2017) 7–17.
[34] S. Kashani, A. Ranjbar, M. Abdollahzadeh, S. Sebti, Solidification of nano-enhanced phase change material (NEPCM) in a wavy cavity, Heat Mass Transf. 48 (2012) 1155–1166.
[35] M. Abdollahzadeh, M. Esmaeilpour, Enhancement of phase change material (PCM) based latent heat storage system with nano fluid and wavy surface, Int. J. Heat Mass Transfer 80 (2015) 376–385.
[36] M. Jourabian, M. Farhadi, A.R. Darzi, Simulation of natural convection melting in an inclined cavity using lattice Boltzmann method, Scientia Iranica 19 (2012) 1066–1073.
[37] R. Sharma, P. Ganesan, J. Sahu, H. Metselaar, T. Mahlia, Numerical study for enhancement of solidification of phase change materials using trapezoidal cavity, Powder Technol. 268 (2014) 38–47.
[38] B. Kamkari, H. Shokouhmand, F. Bruno, Experimental investigation of the effect of inclination angle on convection-driven melting of phase change material in a rectangular enclosure, Int. J. Heat Mass Transfer 72 (2014) 186–200.
[39] H. Zennouhi, W. Benomar, T. Kousksou, A.A. Msaad, A. Allouhi, M. Mahdaoui, T. El Rhafiki, Effect of inclination angle on the melting process of phase change material, Case Stud. Thermal Eng. 9 (2017) 47–54.
[40] L. Zeng, J. Lu, Y. Li, W. Li, S. Liu, J. Zhu, Numerical study of the influences of geometry orientation on phase change material's melting process, Adv. Mech. Eng. 9 (2017) 1687814017720084.
[41] N.S. Dhaidan, Nanostructures assisted melting of phase change materials in various cavities, Appl. Therm. Eng. 111 (2017) 193–212.
[42] N.S. Dhaidan, Melting phase change of n-eicosane inside triangular cavity of two orientations, J. Renewable Sustainable Energy 9 (2017) 054101.
[43] J. Zhao, J. Zhai, Y. Lu, N. Liu, Theory and experiment of contact melting of phase change materials in a rectangular cavity at different tilt angles, Int. J. Heat Mass Transfer 120 (2018) 241–249.
[44] I. Al Siyabi, S. Khanna, T. Mallick, S. Sundaram, An experimental and numerical study on the effect of inclination angle of phase change materials thermal energy storage system, J. Energy Storage 23 (2019) 57–68.

[45] X. Yang, Z. Guo, Y. Liu, L. Jin, Y.-L. He, Effect of inclination on the thermal response of composite phase change materials for thermal energy storage, Appl. Energy 238 (2019) 22–33.
[46] F. Iachachene, Z. Haddad, H.F. Oztop, E. Abu-Nada, Melting of phase change materials in a trapezoidal cavity: Orientation and nanoparticles effects, J. Mol. Liq. (2019).
[47] N.S. Bondareva, B. Buonomo, O. Manca, M.A. Sheremet, Heat transfer performance of the finned nano-enhanced phase change material system under the inclination influence, Int. J. Heat Mass Transfer 135 (2019) 1063–1072.
[48] S. Motahar, N. Nikkam, A.A. Alemrajabi, R. Khodabandeh, M.S. Toprak, M. Muhammed, A novel phase change material containing mesoporous silica nanoparticles for thermal storage: a study on thermal conductivity and viscosity, Int. Commun. Heat Mass Transfer 56 (2014) 114–120.
[49] F. Wang, W. Lin, Z. Ling, X. Fang, A comprehensive review on phase change material emulsions: Fabrication, characteristics, and heat transfer performance, Sol. Energy Mater. Sol. Cells 191 (2019) 218–234.
[50] S.A.M. Mehryan, A. Tahmasebi, M. Izadi, M. Ghalambaz, Melting behavior of phase change materials in the presence of a non-uniform magnetic-field due to two variable magnetic sources, Int. J. Heat Mass Transfer 149 (2020) 119184.
[51] M. Ghalambaz, S.M. Hashem Zadeh, S.A.M. Mehryan, K. Ayoubi Ayoubloo, N. Sedaghatizadeh, Non-Newtonian behavior of an electrical and magnetizable phase change material in a filled enclosure in the presence of a non-uniform magnetic field, Int. Commun. Heat Mass Transfer 110 (2020) 104437.
[52] O. Schenk, K. Gärtner, Solving unsymmetric sparse systems of linear equations with PARDISO, Future Generat. Comput. Syst. 20 (2004) 475–487.
[53] P. Wriggers, Nonlinear Finite Element Methods, Springer Science & Business Media, 2008.
[54] F. Verbosio, A. De Coninck, D. Kourounis, O. Schenk, Enhancing the scalability of selected inversion factorization algorithms in genomic prediction, J. Comput. Sci. 22 (2017) 99–108.
[55] M.H. Matin, W.A. Khan, Laminar natural convection of non-Newtonian power-law fluids between concentric circular cylinders, Int. Commun. Heat Mass Transfer 43 (2013) 112–121.
[56] H. Cheong, Z. Siri, S. Sivasankaran, Effect of aspect ratio on natural convection in an inclined rectangular enclosure with sinusoidal boundary condition, Int. Commun. Heat Mass Transfer 45 (2013) 75–85.
[57] C. Gau, R. Viskanta, Melting and solidification of a pure metal on a vertical wall, J. Heat Transfer 108 (1986) 174–181.
[58] A. Brent, V. Voller, K. Reid, Enthalpy-porosity technique for modeling convection-diffusion phase change: application to the melting of a pure metal, Numer. Heat Trans. Part A Appl. 13 (1988) 297–318.
[59] K. Kahveci, Buoyancy driven heat transfer of nanofluids in a tilted enclosure, J. Heat Trans. 132 (2010) 062501.